RSC Advances

PAPER

View Article Online
View Journal | View Issue

Cite this: *RSC Adv.*, 2024, **14**, 29260

Efficient energy and memory storage capabilities in optimized $BiFeO_3/MnMoO_4/NiFe_2O_4$ triphasic composites for futuristic multistate devices

Izhar Sagheer, *[a] Muhammad Tamoor Ansar,[b] Shahid M. Ramay,[c] Houbing Huang[de] and Shahid Atiq *[a]

The emergence of multiferroic materials particularly bismuth iron oxide ($BiFeO_3$) with distinctive magnetoelectric, and high energy storage capabilities, present pivotal aspects for next-generation memory storage devices. However, intrinsically weak magnetoelectric coupling limits their widespread applications, that can be leap over by the integration of $BiFeO_3$ with enriched ferroelectric, and ferro/ferrimagnetic materials. Here, a series $(1-x)[0.7BiFeO_3 + 0.3MnMoO_4] + xNiFe_2O_4$ (x = 0.00, 0.03, 0.06, and 0.09) is synthesized *via* citrate-gel based self-ignition, and solid-state reaction routes. Phase purity and crystallinity of tri-phase composites with surfaces revealing random and arbitrarily shaped grains are assured by X-ray diffraction, and field emission scanning electron microscopy, respectively. Dielectric studies illustrated non-linear trend for broad range of frequencies as predicted by Maxwell–Wagner theory along with single semicircle arcs in Nyquist plots that exposes grain boundaries effect. An enriched 68.42% of ferroelectric efficiency is featured for x = 0.06 substitutional contents, while magnetic computations demonstrated improved saturation magnetization (M_s), remanence magnetization (M_r), and coercive applied magnetic field (H_c) values as 5.87 emu g^{-1}, 0.96 emu g^{-1}, and 215.19 Oe, respectively for x = 0.09 phase-fraction. The intriguing linear trends of magnetoelectric coupling for all the compositions are corroborating them propitious contenders for futuristic multistate devices.

Received 18th July 2024
Accepted 7th September 2024

DOI: 10.1039/d4ra05223d

rsc.li/rsc-advances

1. Introduction

Multiferroic (MF) single phase ceramics have attracted noteworthy attention owing to their extraordinary electric properties and the coexistence of one or more distinct ferroic orders (ferroelectricity (FE), ferromagnetism (FM), ferroelasticity, and ferrotoroidicity).[1] Miniaturization of MF-based low power and advanced multifunctional devices are the need of the hour as such devices can afford viable utilization in clean energy storage, water purification and medical treatment applications.[2–4] Among multiple-ferroic order materials, magnetoelectric (M–E) materials have combinations of ferroelectric and ferromagnetic orders that can be switched by the applied electric as well by the magnetic field. That's why, these materials make imperative part of multifunctional devices *e.g.*, energy storage, spintronics, transducers and sensors. In addition, coupling between electric and magnetic orders is far important to design four logic state storage devices which is the future of memory storage devices.[5] However, the coupling must be strong enough to have well controlled domains by corresponding as well noncorresponding field.

Amongst all MF materials, $BiFeO_3$ (BFO) has been declared as the only known significant material to have MF property even at room temperature (RT) with 640 K and 1100 K as Néel temperature (T_N) and ferroelectric Curie temperature (T_c), respectively,[6] exhibiting rhombohedral distorted cubic perovskite structure with general formula ABO_3.[7] Its FE trend is majorly due to lone pairs or distortion in bonds that produces relatively weak coupling between both orders; thus, outcome in lower ferroelectricity, high leakage current, weak remanent polarization and magnetization drawbacks. To overcome these shortcomings, MF-based manganese molybdenum tetra oxide $MnMoO_4$ (MMO) having monoclinic type structure is preferred that can effectively upsurge the FE order of the BFO.[8] MMO is a mesoporous material as well, hence, it is very suitable to introduce well-porous ability in composites for potential storage applications.[9] However, the magnetic property is optimized by the substitution of spinel-phased $NiFe_2O_4$ (NFO).

[a]*Centre of Excellence in Solid State Physics, University of the Punjab, Lahore 54590, Pakistan. E-mail: izhar.phd.cssp@pu.edu.pk; satiq.cssp@pu.edu.pk*
[b]*School of Engineering and Built Environment, Griffith University, Parklands Drive, Gold Coast, Queensland 4222, Australia*
[c]*Physics and Astronomy Department, King Saud University, Riyadh, Saudi Arabia*
[d]*School of Materials Science and Engineering, Beijing Institute of Technology, Beijing 100081, China*
[e]*Advanced Research Institute of Multidisciplinary Science, Beijing Institute of Technology, Beijing 100081, China*

Spinel ferrites have emerged as the most suitable magnet phases to be used in tri-phasic MF composites. These ferrites possess general formula AB_2O_4, where A is a divalent cation while B is a trivalent cation. In the present case, Fe^{3+} is trivalent cation (B), while Ni^{2+}(A) is a divalent cation. Spinel ferrites are selected due to their exceptional properties like high saturation magnetization (M_s) values, low eddy current losses, large magneto-crystalline anisotropy, high T_c, excellent squareness ratio, low coercivity (H_c) values, mechanical hardness and high electric resistivity. In our case, NFO was preferred due to its high resistivity, exceptional permeability and enriched M_s values.[10]

In 2019, Khan *et al.*, substituted NFO to $BaTiO_3$ synthesized by sol–gel auto-combustion mechanism and found reduction in band gap with increase in NFO concentrations.[11] Mn-doped MF-composites were developed by sol–gel self-ignition approach to have magnetically softened and very low coercive materials by Dhanalakshmi *et al.*[12] In another work, increasing contents of spinel ferrites resulted into great impact on BFO ME-coupling to face BFO challenge of low antiferromagnetic order by preparing the samples *via* reliable synthesis *i.e.*, sol–gel auto-combustion process by Umair and his co-workers.[13] In another study, Ali and his group synthesized tri-phase composites by citrate-gel self-combustion approach followed by solid-state mechanism with tunable FE and magnetization for ultra-sensitive devices along with their fast switching and excellent ME-couplings.[14] Augustine and co-workers also synthesized two phase composites of BFO and spinel ferrites by citrate-gel auto-ignition route and achieved significantly improved coupling of magnetic and ferroelectric orders.[15] Interestingly, BFO-PVDF-CB (carbon black) composites with various weight percentages of CB sanctioned high dielectric constant with suppressed dielectric losses by synthesizing *via* solution casting technique by Moharana *et al.*[16] Two phases of BFO and PZT (lead zirconate titanate) were dispersed in various weights of PVDF (poly vinylidene fluoride) to have a tri-phase composite by sol–gel auto-combustion and ball-milling methods that presented decreasing polarization while coercivity was found to increase. In addition, ME-coupling was also significantly improved by Mehak *et al.*[17] Unique kinds of composites were synthesized by Sreekanth *et al.*, using cost effective sol–gel self-ignition method, those were nano as well bulk composites. Compellingly, both samples showed super-paramagnetic behavior at RT with coercivities close to zero.[18] In March 2023, tri-phasic BFO–$BaTiO_3$–$MnFe_2O_4$ composites were orchestrated by urea-glycine based self-ignited sol–gel mechanism for highly efficient and strong magnetoelectric coupling based ultrasensitive devices.[19] In all above works, porosity and ME couplings were not targeted to enhance simultaneously.

Considering deficiencies in previous efforts, in this project; shortcomings are tried to overcome. Hence, this work emphasis on the synthesis of two phases *i.e.*, BFO and NFO by citrate-gel followed by auto-ignition process while third MMO phase is prepared by solid-state mechanisms and then composite series $(1-x)$[0.7BFO + 0.3MMO] + xNFO with $x = 0.00$, 0.03, 0.06, and 0.09 substitutional contents is routed through solid-state approach. In studied literature, all the researchers reported their individual efforts for electric polarization and magnetic responses while current study summarizes couplings of three phases for practical applications in energy storage and generation as well in ultra-fast switching memory devices.

2. Experimental

The targeted series $(1-x)$[0.7BFO + 0.3MMO] + xNFO with $x =$ 0.00, 0.03, 0.06, and 0.09 substitutional contents are synthesized by different mechanisms as elaborated in Fig. 1(a–c). For better crystallinity outcomes, BFO and NFO were prepared by

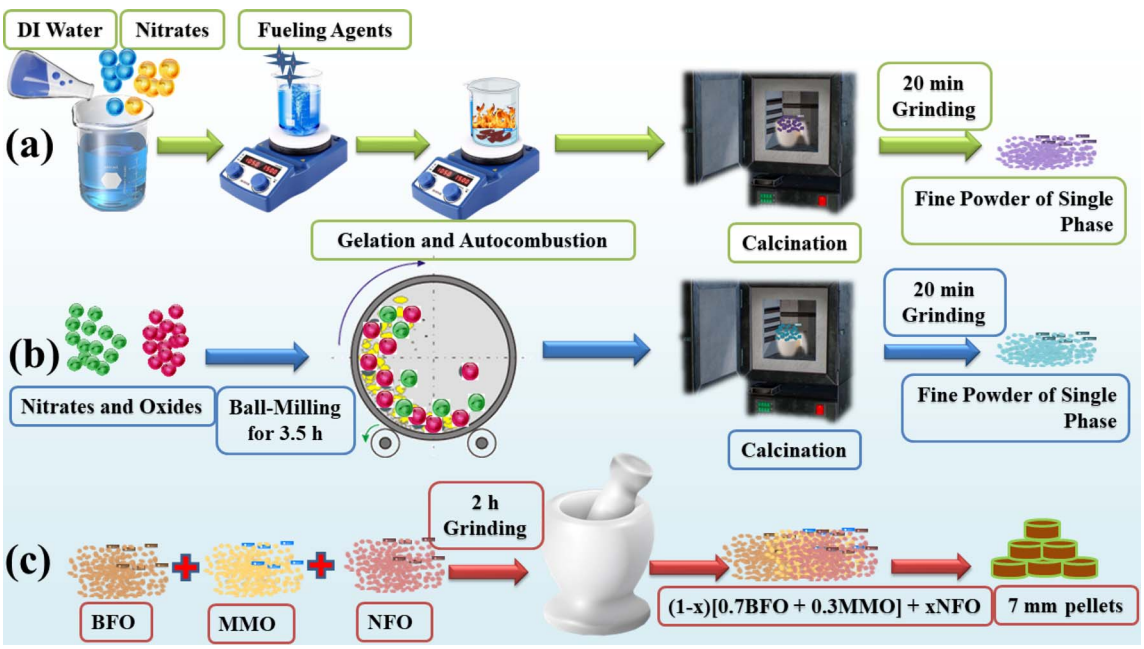

Fig. 1 Schematics sample synthesis of (a) BFO and NFO by citrate-gel self-ignition approach, (b) MMO by solid-state route, and (c) composite preparation by grinding process.

cost-effective and bottom-up citrate-gel auto-ignition process as depicted in Fig. 1(a). For this purpose, nitrate precursors were preferred due to their good solubility in deionized (DI) water,[20] hence, stoichiometric quantities of bismuth nitrate pentahydrate [$Bi(NO_3)_3 \cdot 5H_2O$], iron nitrate nonahydrate [$Fe(NO_3)_3 \cdot 9H_2O$] and nickel nitrate hexahydrate [$Ni(NO_3)_2 \cdot 6H_2O$] with high purity ≥99% (purchased from Sigma Aldrich) were consumed for specimen synthesis. Initially, relative proportions of [$Bi(NO_3)_3 \cdot 5H_2O$] and [$Fe(NO_3)_3 \cdot 9H_2O$] were dissolved in DI water to make homogenous solutions. Small amount of HNO_3 was added to [$Bi(NO_3)_3 \cdot 5H_2O$] solution for better solubility.[21] These two solutions were mixed in a single large beaker, afterwards, fueling agents including urea (CH_4N_2O) and glycine ($C_2H_5NO_2$) (with 1.5 : 1, respectively) were poured to metal nitrates. Then, the beaker was positioned on a hot plate with magnetic stirrer inside the beaker for smooth stirring of the solutions. Similar procedure was adopted with [$Ni(NO_3)_2 \cdot 6H_2O$] and [$Fe(NO_3)_3 \cdot 9H_2O$] without addition of HNO_3. Both solutions formed gel-like stuff after being heated at 100 °C for 1 h along with stirring. After gel formation, temperature was increased gradually with time interval of 3 min and 25 °C upsurge in temperature until auto-combustion occurred. The solution with BFO contents got combustion at 275 °C solution whilst with NFO concentrations got ignition at 250 °C. Additional heat treatments transformed them to dry ashes finally. Conversely, owing to the insolubility of molybdenum oxides in water, solid-state route is preferred for the synthesis of MMO in which manganese nitrate tetrahydrate [$Mn(NO_3)_2 \cdot 4H_2O$] and molybdenum trioxide [MoO_3] were utilized as precursors.[22] Consistent with their stoichiometric ratios, the as-mentioned precursors were placed in a ball-mill machine and milled for 3 h and 30 min for each with a time span of 30 min as illustrated in Fig. 1(b).

Afterwards, BFO, MMO and NFO specimen were positioned in ceramic crucibles, and then, crucibles were placed in a box furnace and calcined separately for 3 h at 550 °C, 800 °C, and 800 °C temperatures, respectively.[23] Calcination process developed the desired crystal structures of the constituent phases. Subsequently, three samples were ground separately for 20 min each to get the fine powders. Then, these phases were mixed together consistent with the composition ratios as $x = 0.00$, 0.03, 0.06, and 0.09 in $(1 - x)$[0.7BFO + 0.3MMO] + xNFO series, by separately grinding the composites for 2 h of each using mortar and pestle as demonstrated in Fig. 1(c). Griding was done slowly, so that particle structure or shape would not be affected.[24] Fine powders of composites were pressed by apex hydraulic press with the force of 30 kN to make the uniform pellets of 7 mm in diameter and 1.1 mm of thicknesses because most analyses are performed in pellets form. The dimensions of pellets were measured using vernier caliper and measure scale (FA/JA series) respectively, for all the as-synthesized concentrations.

Crystal structures of the as-formed composites were determined by X-ray Diffractometer (XRD) analysis, and to do so, Powder XRD, Equinox 2000, Thermo Fisher Scientific USA was employed. Surface features were probed using field emission scanning electron microscopy (FESEM) *via* America ixrf (model # 550i) with 200 00× magnification and Java scripted ImageJ software was used to perceive the particles shapes, voids and size distribution. Exact stoichiometric ratios of the elements in various composites were measured by energy dispersive X-ray spectroscopy (EDX) and in addition; elemental mapping of the separate constituent elements was also done using EDX. Dielectric, impedance spectroscopic, ac-conductivity (σ_{ac}) and electric modulus analysis were conducted by 6500B Wayne Kerr impedance analyzer that examines the material's response to sinusoidally varying electric field (EF).[25] Pellets were positioned between two copper electrodes and frequency dependent (20 Hz–20 MHz) series and parallel capacitance, resistance, reactance and impedance responses of the materials were recorded by applying EF.

Being a complex quantity, real (M') and imaginary (M'') parts of electric modulus were determined by following relations.[26]

$$M' = \varepsilon'/(\varepsilon' + \varepsilon'')^2 \quad (1)$$

$$M'' = \varepsilon''/(\varepsilon' + \varepsilon'')^2 \quad (2)$$

Highly advanced and accurate DXV-9000 series vibrating sample magnetometer (VSM) was operated to get magnetic responses of the materials to the applied magnetic field.

Multiferroic analyzer (Radiant's Tech. USA) was employed for specific ferroelectric as well magnetoelectric characterizations like polarization–electric field (PE) loops and M–E coupling effects in tri-phase composites. Voltage was kept in between 10 to 80 V. The scrutinized results and then their precise calculations are mentioned in results and discussion.

3. Results and discussion

The impressions of atomic arrangements *i.e.*, crystalline structures within the series $(1 - x)$[0.7BFO + 0.3MMO] + xNFO with x = 0.00, 0.03, 0.06, and 0.09 phase-fractions were determined using Cu-K_α radiations having 1.5406 Å of wavelength. The detector recorded the XRD patterns within 2θ range of 10°–90° and the relative peaks positioned at various angular positions were indexed by the analytical approach proposed by B. D. Cullity.[27] The indexed XRD patterns are profiled in Fig. 2(a) in which the intense peaks attributed to BFO phase with lattice planes (100), (110), (1$\bar{1}$0) and (2$\bar{2}$1) traced at 22.81°, 32.33°, 32.45° and 71.81° angular positions, respectively. These indexed BFO patterns were perceived to be promising with ICSD reference # 01-072-2035 that confirmed the development of rhombohedral perovskite structure having *R*3*c* space group. Fig. 2(b) depicts the emergence of twin peaks of BFO at (110) and (1$\bar{1}$0) crystal planes which confirmed the existence of high crystallinity of BFO phase. Similarly, the peaks emerged at $2\theta = 26.02°$, 40.10°, 46.38°, 49.67°, 52.14°, 52.38°, 57.16°, 57.34°, 67.34°, 67.86°, 71.96°, 72.14°, 72.57°, 75.59°, 77.03°, and 80.82° corresponding to (002), (041), (042), (4$\bar{2}$3), (133), (5$\bar{3}$1), (024), (114), (7$\bar{1}$3), (550), (2$\bar{6}$3), (622), (063), (8$\bar{2}$2), (154), and (2$\bar{0}$6) Bragg's planes, respectively that confirmed the MMO formation. The indexed peaks were in agreement with ICSD reference # 01-072-0285 illustrated the existence of monoclinic crystal structure

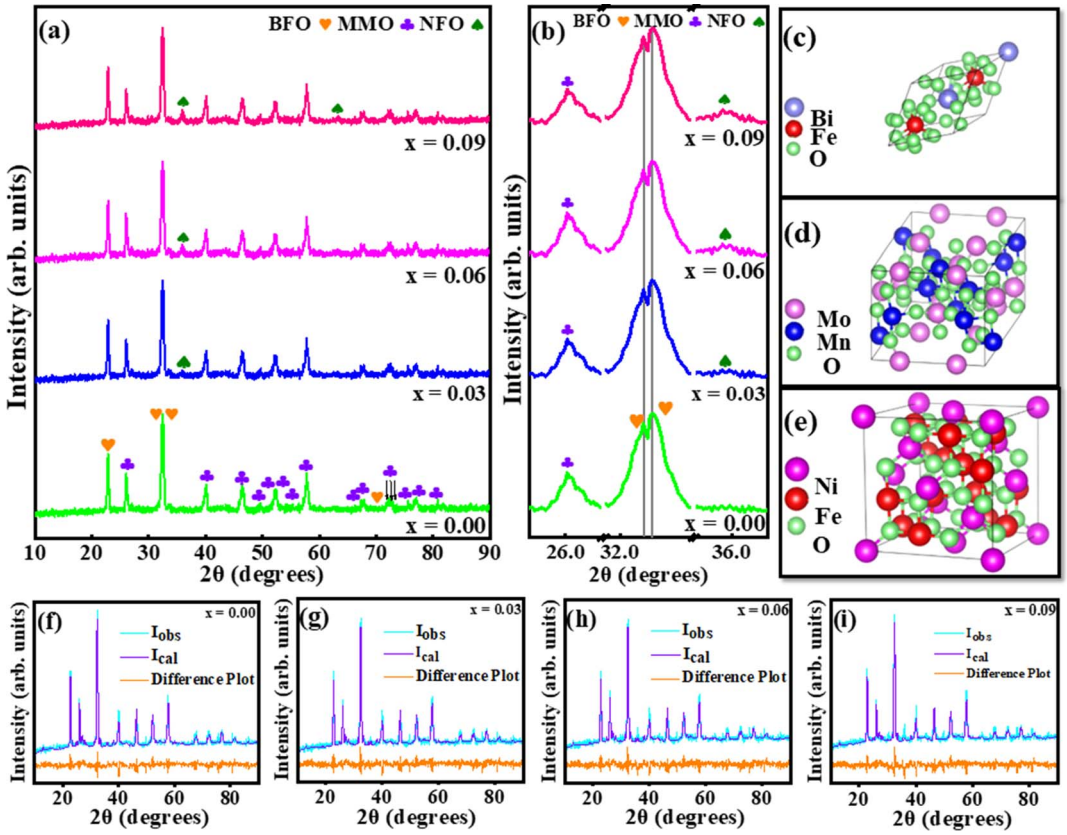

Fig. 2 (a) XRD patterns of $(1-x)$[0.7BFO + 0.3MMO] + xNFO with $x = 0.00$, 0.03, 0.06, and 0.09 phase-fractions, (b) BFO twin peaks, crystal structures of (c) BFO, (d) MMO, and (e) NFO, Rietveld refinement patterns for (f) $x = 0.0$, (g) $x = 0.03$, (h) $x = 0.06$, and (i) $x = 0.09$ composites.

with $C2/m$ space group. In addition, indexed peaks at 35.88° and 63.34° angular positions attributed to (311) and (440) lattice planes, respectively that assured the existence of NFO cubic spinel structure in the specimen for $x > 0.00$ substitutional contents and matched with ICSD reference # 01-074-2081 with space group $Fd3m$. The sample with $x = 0.00$ concentration is comprising of BFO and MMO phases while with $x > 0.00$ phase-fractions consists of tri-phases as evident by XRD patterns in which peaks of NFO became intensified by increasing NFO concentrations, demonstrating the increased crystallinity. Interestingly, peaks of BFO and MMO are not affected appreciably by the increasing concentrations and no extra peaks were appeared promising the existence of pure phases of the specimen.[28]

The Scherrer's approach was used to determine the crystallite sizes (D_{hkl}) for each phase in all the samples. D_{hkl} for BFO and MMO depicts minute variations for different phase-fractions, however, NFO behaved in a unique way for its relevant substitutional contents. Herein, D_{hkl} values for NFO is largest for $x = 0.03$ substitutions and approximately same for other contents ($x = 0.06$, and 0.09). Scherrer's formula is given as,[29]

$$D_{hkl} = \frac{k\lambda}{\beta \cos \theta_B} \quad (3)$$

where, 'k' determines the shape factor that is Scherrer constant bearing a value of 0.9, 'λ' is wavelength of incident Cu-K_α radiations (1.5406 Å), 'β' gives full width at half maxima (FWHM) (radians), while 'θ_B' determines Braggs angle. Bulk density ($\rho_B = m/V$) or experimental density predicts the mass per unit volume of the composite pellets and is taken in g cm^{-3}. X-ray density ($\rho_x = NM/N_A V_C$ with N: number of formula units, M: molecular weight, N_A: Avogadro's number and V_C: volume of unit cell) or theoretical density defines the density of the material without defects. Porosity (%) for all the samples is calculated by the eqn (4).[30]

$$\text{Porosity}(\%) = 1 - \frac{\rho_B}{\rho_x} \times 100 \quad (4)$$

Table 1 enlists the values of lattice parameters (a, b and c), D_{hkl}, ρ_B, ρ_x and porosities (%) relative to different concentrations ($x = 0.00$, 0.03, 0.06, and 0.09 phase-fractions). Maximum porosity is evident for $x = 0.06$ concentration specifying its applications in sound absorption, heat insulation and energy storage, and mechanical-to-electrical energy conversion devices,[31] as the greater active area of the material offers more place to store charges. Using determined parameters; crystal structures of BFO, MMO and NFO were designed using Vesta software and are revealed in Fig. 2(c)–(e), respectively.

Table 1 Lattice parameters, average crystallite size (D_{hkl}), bulk density (ρ_B), X-ray density (ρ_X), and percentage porosity for $(1-x)$[0.7BFO + 0.3MMO] + xNFO with $x = 0.00$, 0.03, 0.06, and 0.09 composites

NFO contents (x)	Lattice constants (Å)					D_{hkl} (nm)			ρ_B (g cm^{-3})	ρ_X (g cm^{-3})	Porosity (%) ± 2%
	BFO	MMO			NFO						
	$a = b = c$	a	b	c	$a = b = c$	BFO	MMO	NFO			
0.00	3.96	10.47	9.52	7.14	Nil	31	25	—	3.97	7.11	44
0.03	3.96	10.47	9.52	7.14	8.30	32	24	92	4.11	7.05	42
0.06	3.96	10.47	9.52	7.14	8.30	32	25	74	3.18	7.00	54
0.09	3.96	10.47	9.52	7.14	8.30	32	24	76	4.03	6.95	42

Table 2 Rietveld's refined structural parameters for $(1-x)$[0.7BFO + 0.3MMO] + xNFO for $x = 0.00$, 0.03, 0.06, and 0.09 composites

NFO contents (x)	0.00	0.03	0.06	0.09
R_{exp}	20.0	19.64	18.72	18.45
R_p	6.93	7.06	6.48	6.25
R_{wp}	8.83	8.94	8.27	8.14
$D_{statistics}$	0.21	0.48	0.46	0.40
W.$D_{statistics}$	0.21	0.53	0.50	0.41
χ^2	0.19	0.21	0.20	0.19

To further depict the purity of composites, Rietveld's refinement analysis was carried out using X'Pert HighScore Plus software. All the involved R-factors like R-profile (R_p), weighted R-profile (R_{wp}) and R-expected (R_{exp}) were determined using the as-mentioned software. The most important factor $\chi^2 = R_{wp}/R_{exp}$ (goodness of fit) was found with its best value. The lowest values of χ^2 unveiled that our experimental consequences are in accordance with calculated values *i.e.*, successful development of composite phases and all the determined Rietveld's refined factors are computed in Table 2. This can also be observed by the graphical representation of Rietveld's refinement shown in Fig. 2(f–i) for all the compositions that clearly demonstrates excellent matching of experimental and theoretical data. Minute differences in the peaks of experimental and theoretical densities are due to existence of defects or vacancies in the specimen.

Morphological features of the concerning series $(1-x)$ [0.7BFO + 0.3MMO] + xNFO with $x = 0.00$, 0.03, 0.06, and 0.09 substitutional contents was achieved by FESEM and illustrated in Fig. 3(a–d). Overall, in these micrographs, surfaces were depicted to be very smooth as pellets were used for scanning and also agglomeration could be perceived due to high pressure while making pellets and magnetic nature of NFO-contents. Various shapes of the grains like rectangular, cubical and irregular are present and grain sizes were averagely ranging between 20–130 nm and are demonstrated by histograms as well. All these variations can be modified by heat treatment conditions while synthesizing the samples. Actually, changing grain and crystallite sizes affect the mean free path of electrons so resistivity is changed by this mechanism to improve our material for certain practical needs.

The existence of various elements is keenly analyzed by elemental mapping that is carried out for $x = 0.03$ and 0.09 substitutions as revealed in Fig. 3(e) and (f), respectively. Colored areas are indicating the presence of an element in that particular area, while dark areas characterize the absence of that particular element. The colored images are attributing various detected X-rays associated with Bi, Fe, Mn, Mo, and Ni.[32] Plots in Fig. 3(g) depicts the relative intensities of X-rays emitted by the elements present in our samples, thus giving the existence of proper stoichiometric ratios of the constituent elements. There are minor changes in the peaks of Bi and Fe for all samples. Ni peaks are hardly observed due to such a small concentration substituted. To further explore the voids depicted in the specimen that directly verify the measured porosity from the pellets are sketched in Fig. 3(h).

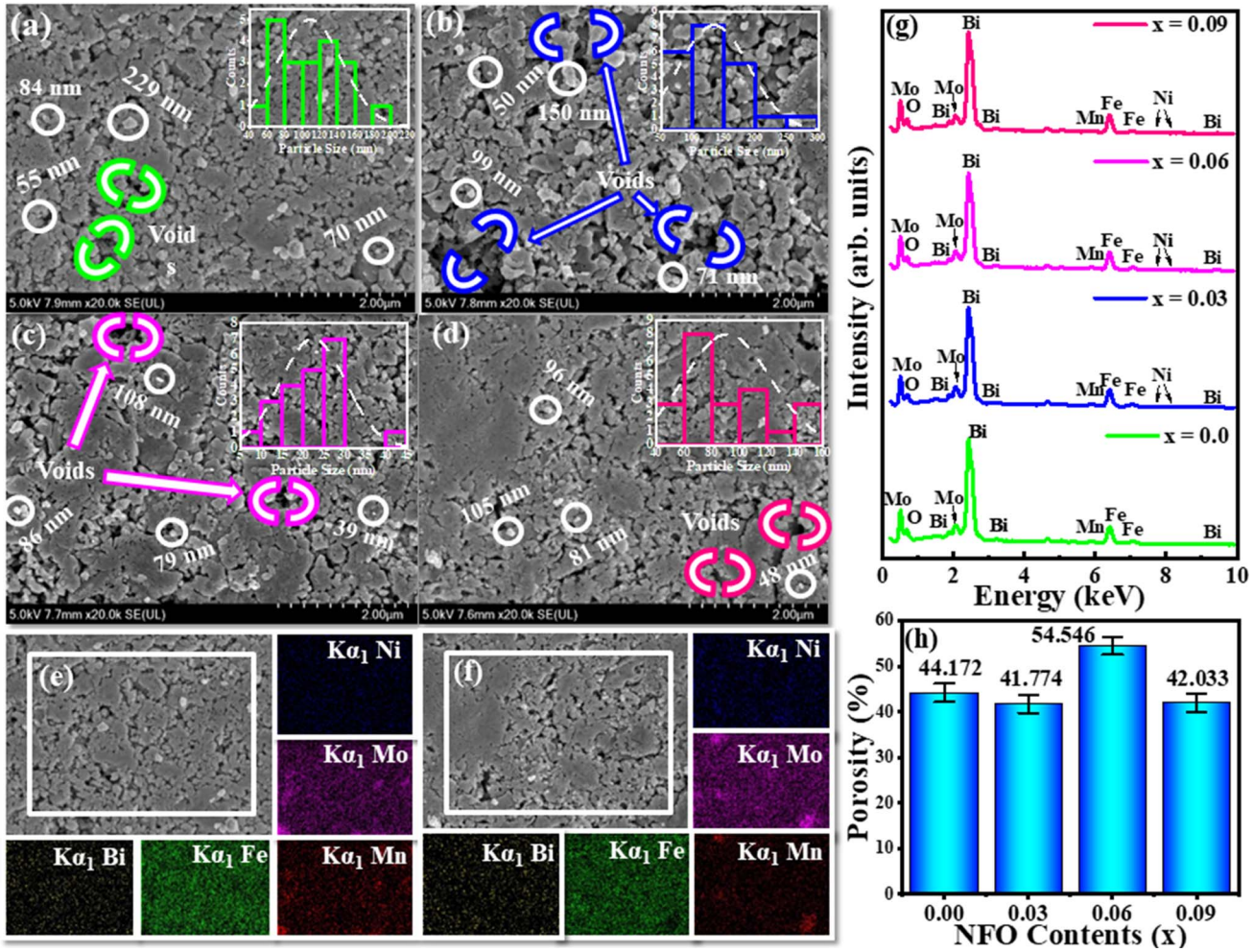

Fig. 3 FESEM images of $(1-x)$[0.7BFO + 0.3MMO] + xNFO triphasic composites for x = (a) 0.00, (b) 0.03, (c) 0.06 and (d) 0.09, X-ray mapping for x = (e) 0.00 and (f) 0.09, (g) EDX pattern and (h) percentage porosities for all concentrations.

Dielectrics are expected to have no free electrons ideally to perform polarization operation under the action of EF and dipoles switching are responsible for storing electrical energy. In fact, polarization is directly affected by temperature and frequency of varying applied EF as well. Hence, real (ε') and imaginary (ε'') parts of dielectrics are determined using $\varepsilon' = C_p d/A\varepsilon_o$ and $\varepsilon'' = \varepsilon' \tan\delta$, where $\tan\delta$ is tangent loss determined by $\tan\delta = 1/(2\pi fCR)$. The variations in ε' and ε'' *versus* log of frequency ($\log f$) for the series $(1-x)$[0.7BFO + 0.3MMO] + xNFO (with x = 0.00, 0.03, 0.06, and 0.09 substitutional contents) are illustrated in Fig. 4(a) and (b), respectively. For low frequency region, high ε' as well as high ε'' trend was perceived, whilst trend changes gradually to lowest constant values in high frequency ranges. This behavior is usually associated with ferrites as they response in such a way to extremely fast fluctuating EF.[33]

In real, low frequency is very suitable for all kind of polarizations (electronic, atomic, space charge and orientational) to occur that also support each other, however; going towards high frequency domains, electronic and atomic polarizations start to takeover other two polarizations because it is not possible for space charge and orientational polarizations to response rapidly with varying EF. In all kind of polarizations, response of material is measured by relaxation time $\tau = 1/(2\pi f_c)$ that is the time in which the dipole switches in the retort of applied EF. Interestingly, Koop's theory as well as Maxwell–Wagner model support such a fluctuating behavior. According to Maxwell–Wagner model, conduction between conducting grains is prohibited by insulating grain boundaries. Polarization occurs by self-orientation of charges along the boundaries and results into upsurge of dielectric parameters. Charges follow the fluctuating EF but as the frequency increases; it become more difficult for charges to trail the applied field; hence, dielectric parameters reduce to lower values. Essentially, electrons and holes approach the grain boundaries by hopping phenomenon and these observations are also accredited to substitution of NFO contents. As the concentration is increased, the probability of hopping through grain boundaries increases; consequently, for greater NFO concentration, enriched dielectric parameters were perceived. Energy is stored in the material due to its response to applied EF and when that energy is taken back, small part of that is lost as heat which is declared as tangent

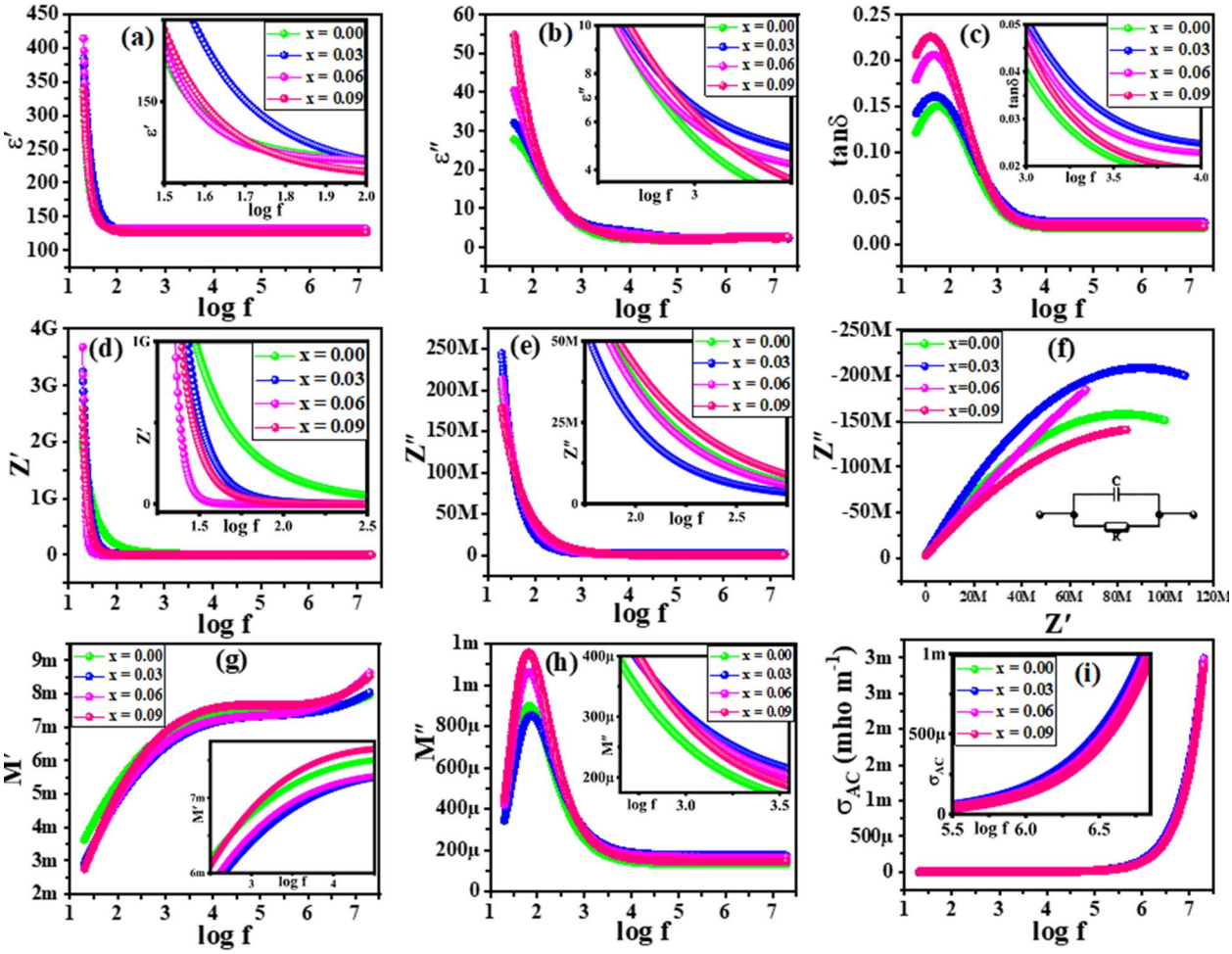

Fig. 4 Variation in (a) real, (b) imaginary part of dielectric constant, (c) tangent loss (d) real, (e) imaginary parts of impedance w.r.t. log of frequency, (f) Nyquist plot, (g) real (h) imaginary parts of electric modulus, and (i) *ac* conductivity w.r.t. log of frequency.

loss (tan δ). Empirically, charge hopping and crystal defects are reasons for such heat losses and are plotted in Fig. 4(c). In fact, this plot is in very good agreement with previous plots of Fig. 4(a) and (b), as in low frequency region; due to very active response of grain boundaries, loss is highest according to Maxwell–Wagner model as well as to Koop's theory. However, in high frequency region; energy is lost due to delay in the orientational changes for conduction phenomenon of locally bound charges.

To further evaluate the grains and grain boundaries effect, complex impedance (Z^*) tool is utilized ($Z^* = Z' + iZ''$). This analysis makes a connection between the microstructure and impedance responses, and accordingly, electrical effects of impurities are also envisioned. It exhibits real (Z') and imaginary (Z'') parts.

Fig. 4(d) and (e) are depicting the variations in resistive (Z') and reactive (Z'') responses *versus* log f, respectively for all the specimen. The compositions are attributing declining trend as frequency changes from low to high regime because grain boundaries are most influential; hence, high impedances at low frequency regions were affirmed. In addition, enrichment in concentrations of NFO introduce additional charge carriers in the specimen that take part in the conduction mechanism; accordingly, resistivity decreases and likewise, Z'' follows the identical trend.

Characterization of various phases of samples is done by drawing Z' against Z'' *i.e.*, Nyquist plots and are profiled in Fig. 4(f). Typically, this kind of plot consists of three semicircular arcs, where first one being contributed by grain boundaries, second one by grains, while the third one denotes the electrode effects. Actually, such semicircles are observed if and only if, bulk material has lower resistance as compared to grain boundaries.[26] Generally, this happens due to the maximum resistance at low frequency due to carrier at grain boundaries and less resistance at high frequency is credited by inner grains. In present case, only one semicircle was observed which is indicating grains boundaries effect and single relaxation phenomenon. Further, increased NFO-contents led to decrease the semicircular arc accrediting enriched conductivity due to additional charge carriers. Every semicircle in Nyquist plot can be described by a parallel RC-circuit as shown in the inset of Fig. 4(f). Resistances (R) can be estimated from the intercept of the plots on horizontal axis (Z'), while capacitances (C) can be calculated from using, $2\pi f_{max}RC = 1$. However,

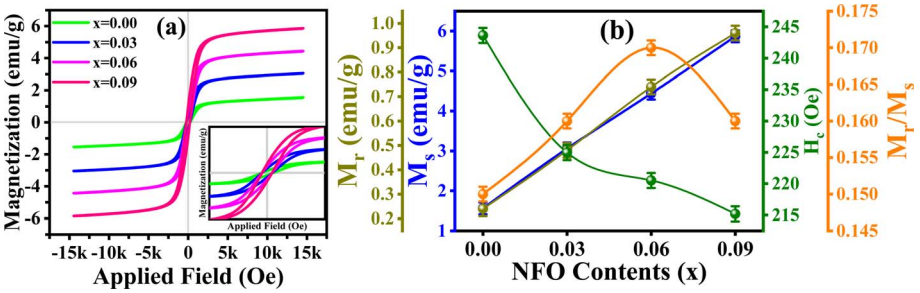

Fig. 5 (a) MH loops of $(1-x)$[0.7BFO + 0.3MMO] + xNFO triphasic composites for $x = 0.00$, 0.03, 0.06 and 0.09, (b) saturation magnetization (M_s), remanence magnetization (M_r), squareness ratio (M_r/M_s) and coercive field (H_c) w.r.t. substitution contents (x).

Table 3 Computed values of saturation magnetization (M_s), remanence magnetization (M_r), coercive applied field (H_c), and squareness ratios (M_r/M_s) for $(1-x)$[0.7BFO + 0.3MMO] + xNFO with $x = 0.00$, 0.03, 0.06, and 0.09 tri-phase composites

NFO contents (x)	M_s (emu g^{-1}) ± 1%	M_r (emu g^{-1}) ± 1%	H_c (Oe) ± 0.1%	M_r/M_s
0.00	1.56	0.24	243.64	0.15
0.03	3.06	0.48	224.97	0.16
0.06	4.44	0.74	220.52	0.17
0.09	5.87	0.96	215.19	0.16

relaxation time (τ) can be determined from the relaxation frequencies (peaks of the arcs) using the relation as; $\tau = RC$.

Complex dielectric modulus and ac-conductivity (σ_{ac}) examinations were employed to further investigate the materials for Debye-type relaxation phenomenon. As compared to impedance spectroscopy, complex modulus spectroscopy is more fruitful to distinguish grain boundaries effect and electric polarization. M' and M'' are calculated using eqn (1) and (2) and corresponding plots are displayed in Fig. 4(g) and (h), respectively. M' has a constant response of a vast range of frequencies, while M'' has a resonance peak at 100 Hz, which is due to relaxation phenomenon, afterwards, M'' starts to decline which is pointing to non-Debye relaxation behavior. In fact, M' and M'' are related to ε' and ε'', so it gives comparative energy stored and losses, respectively.

As the conduction is based upon the movement of charge carriers, so electron hopping, space charge distribution, grain boundaries and charge transitions are the main causes for this phenomenon. Total conductivity is summed up as; $\sigma = \sigma_{dc} + \sigma_{ac}$. Where, σ_{ac} is determined using relation, $\sigma_{ac} = 2\pi f \varepsilon_o \varepsilon' \tan\delta$. Here, σ_{dc} is dc-conductivity. Changes in σ_{ac} *versus* log f for all the specimen are sketched in Fig. 4(i). Moving from low to high frequency region, σ_{ac} remains almost constant; which depicts

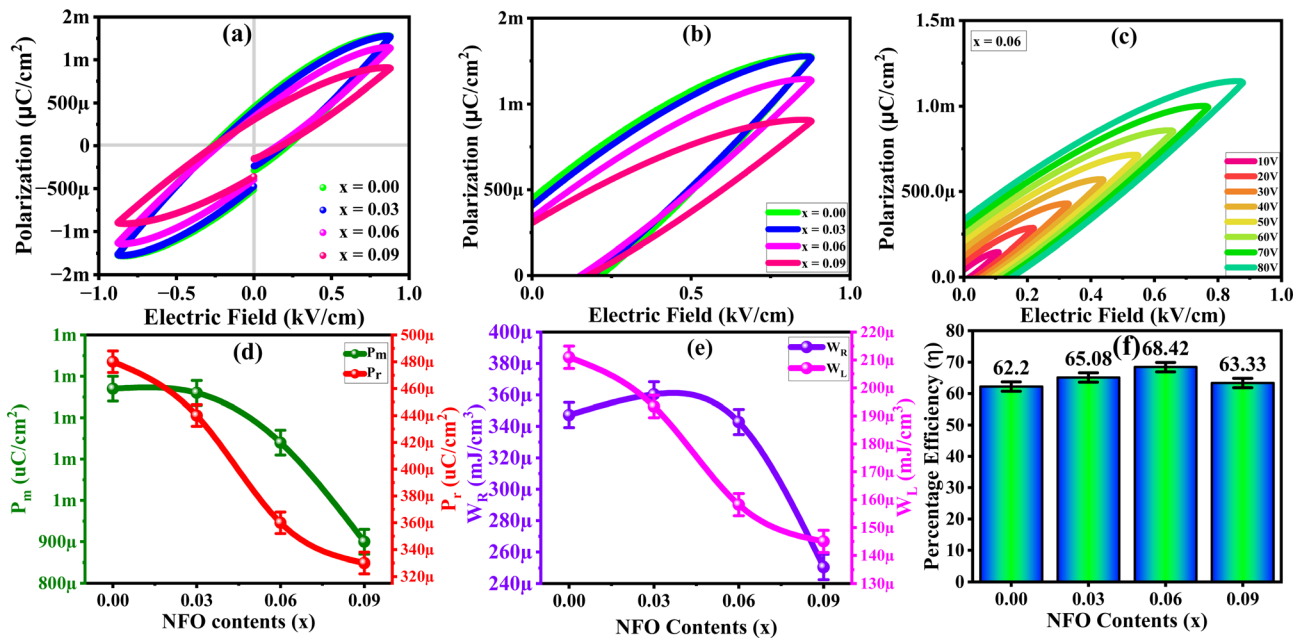

Fig. 6 (a) Polarization (P) *vs.* electric field (E), (b) estimation of energy density by charge–discharge region, (c) charge–discharge observation at various strengths of electric field, (d) saturation/maximum polarization (P_M) and remanence polarization (P_R) for different NFO contents (x), (e) recoverable energy density (W_R) and lost energy density (W_L) for different concentrations of NFO, and (f) energy storage efficiency for various NFO contents (x).

Table 4 Ferroelectric parameters including maximum polarization (P_m), remanence polarization (P_r), coercive electric field (E_c), total energy density (W_T), recoverable energy density (W_R), and energy loss density (W_L) for $(1-x)$[0.7BFO + 0.3MMO] + xNFO with $x = 0.00$, 0.03, 0.06, and 0.09 tri-phase composites

	Ferroelectric parameters						
NFO contents (x)	P_m (μC cm^{-2}) ± 2%	P_r (μC cm^{-2}) ± 2%	E_c (kV cm^{-1}) ± 2%	W_T (mJ cm^{-3}) ± 2%	W_R (mJ cm^{-3}) ± 2%	W_L (mJ cm^{-3}) ± 2%	Percentage efficiency ± 2%
0.00	0.00127	0.00048	0.241	0.000558	0.000347	0.000211	62.20
0.03	0.00126	0.00044	0.217	0.000553	0.000360	0.000193	65.08
0.06	0.00114	0.00036	0.189	0.000501	0.000343	0.000158	68.42
0.09	0.00090	0.00033	0.216	0.000395	0.000251	0.000145	63.33

the frequency-independent behavior (concerning to σ_{dc}). Whilst, in highest frequency regime; increasing trend is perceived due to contribution of free as well as of bound charges which boosts up the conductivity.

To analyze magnetic responses of all the samples, M–H (hysteresis) loops were achieved at ±15 kOe (sketched in Fig. 5(a)), and characteristics like M_s, M_r, H_c, and M_r/M_s were perceived. Deep insight of the plots reveals that all the composites have some spontaneous magnetizations *i.e.*, ferrimagnetism. Graph analysis gives M_s, M_r and H_c, values as 1.56 emu g^{-1}, 0.24 emu g^{-1} and 243.64 Oe, respectively for $x = 0.00$ phase-contents. However, with the introduction of NFO (x = 0.03, 0.06, and 0.09); M_s and M_r increased to 5.87 emu g^{-1} and 0.96 emu g^{-1}, respectively. It may be due to asymmetrical spins present in spinel ferrites which causes enhancement in spontaneous magnetization, while H_c was observed to decrease to 215.19 Oe for highest substituted sample. Exchange coupling interaction of perovskite BFO and spinel NFO is responsible for specific magnetic domains which are in turn responsible for enhancement of ME coupling in composites. The variations in all the computed parameters are profiled in Fig. 5(b) and summarized in Table 3. Further, M_r/M_s values also specifies the ferrimagnetic behavior, however, this ratio is very low and remained approximately same for all the samples.

Ferroelectric materials retain their spontaneous polarization even after the removal of applied electric fields and can switch their polarization under the reversible electric field. The depicted ferroelectric trend characterizes intrinsic properties of the materials and such specimen are probable to revolutionize the energy storage world. Here, ferroelectric behavior of tri-phase composites is investigated by drawing polarization–electric field (*P–E*) loops under ~900 V cm^{-1} of electric field strength and are presented graphically in Fig. 6(a), where all the samples responded unsaturated linear trends under the applied field. *P–E* loops are not closed like magnetic loops, wherein, defect dipoles, polarizability due to ions, grain size, and doping causes leakage current are the main causes for unclosed loops.[34] The dipoles/polarization switching trends (charging/discharging curves) under the variation of applied fields for all the samples in 1st quadrant are displayed in Fig. 6(b) that are further used for the determination of saturation/maximum polarization (P_m), and remanence polarization (P_r). However, coercive electric field (E_c) is also determined for all the specimens. For $x = 0.00$ content, P_m, P_r, and E_c were recorded from the plot as 0.00127 μC cm^{-2}, 0.00048 μC cm^{-2}, and 0.241 kV cm^{-1}, respectively. The inclusion of NFO contents lead to decrease the P_m, P_r and E_c values and for maximum NFO substitution these parameters were computed as 0.00090 μC cm^{-2}, 0.00033 μC cm^{-2}, and 0.216 kV cm^{-1}, respectively. NFO bearing strong magnetic properties, is the cause of reducing trend for ferroelectric parameters. *P–E* curves for $x = 0.06$ substitutional contents under different applied fields are illustrated in Fig. 6(c), while, the variations in P_M and P_R parameters are also revealed graphically in Fig. 6(d). The application of electric field switches electric domains within the material that signifies the energy storage capability. By removing the field, this energy can be recovered and declared as recoverable energy density (W_R). On the other hand, all the stored energy is not recovered completely and lost (W_L) due to frictional losses and electric domain walls motion. Variation in W_R and W_L is shown graphically in Fig. 6(e). In addition, the sum of both energy densities (W_R and W_L) is depicted as total energy density (W_T). In this work, Fig. 6(f) declared sample with $x = 0.06$ phase-fractions as the highest efficient tri-phase composition. The behavior depicted in the Fig. 6(a–f) are pointing towards suitability of the materials for energy as well as data storage devices and all the computed ferroelectric parameters are summarized in Table 4.

The connection between electric and magnetic orders in tri-phase composites are analyzed by M–E coupling phenomenon and are sketched in Fig. 7(a–d). The strength of coupling between the two orders can be justified by exchange interaction between them. The devices having both orders simultaneously can induce electric polarization through the application of magnetic field and the other way round. Application of magnetic field affects the magnetic domains inside the material that outcome in lattice strain, and generates polarization which fluctuates in the same fashion as the applied magnetic field that subsequently produces piezoelectric effect. Herein, the M–E coupling effects in the specimen are just reasonable signals, and are not perfect loops that are linearly fit for better understanding of the trends. In fact, this coupling is indirect as clear from the relation below,

$$M - E \text{ effect} = \frac{\text{Mechanical}}{\text{Electrical}} \times \frac{\text{Magnetic}}{\text{Mechanic}}$$

Hence, by keeping all the results and discussion in mind, it can be concluded that NFO substituted composites are well established to have better coupling between perovskite, and

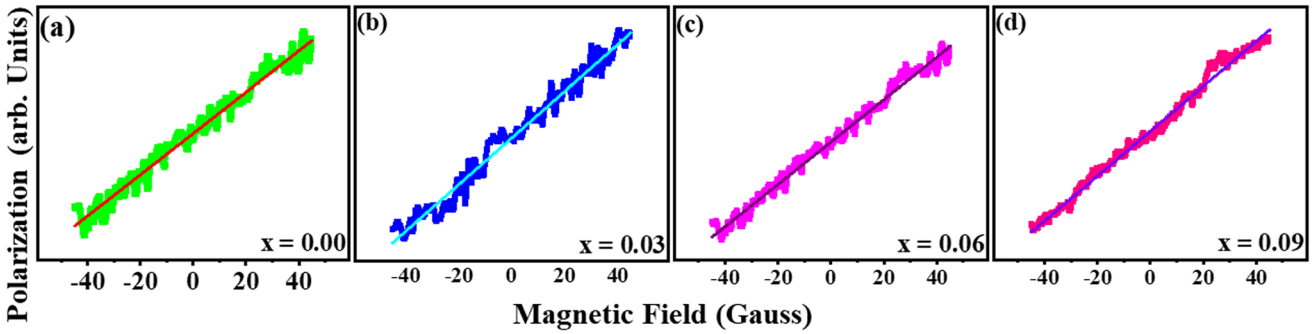

Fig. 7 Magnetoelectric coupling/variation of electric polarization w.r.t. applied magnetic field with NFO contents (a) $x = 0.00$, (b) $x = 0.03$, (c) $x = 0.06$ and (d) $x = 0.09$ in $(1 - x)$[0.7BFO + 0.3MMO] + xNFO triphasic composites.

spinel or between electric and magnetic orders, respectively. Hence, this coupling makes MF appreciable for energy storage, electronic, spintronics, and logic-based states [(P_+, M_+), (P_+, M_-), (P_-, M_+)(P_-, M_-)] devices to read or write the non-volatile data by any field.[35]

4. Conclusion

In a nutshell, this work explores the applicability of a feasible and economical citrate-gel self-ignition and solid-state ball-milling approaches for the synthesis of $(1 - x)$[0.7BFO + 0.3MMO] + xNFO (with $x = 0.00$, 0.03, 0.06, and 0.09 phase-contents) composites. The $x = 0.09$ substitutional contents presented the highest values of dielectric permittivity's well in agreement with Maxwell–Wagner bi-layer model while suppression of polarization phenomenon is accredited by the declining trend of the dielectric constants. The conductivity trends displayed gradually upsurged behavior towards high frequency regime specifying the inclusion of free as well as bound charges towards conduction mechanism. Further, Nyquist plots signified the existence of only one semi-circular arcs attributing the grain boundaries influence. In addition, the tuned magnetic computations validated highest values of M_s and M_r for $x = 0.09$ phase-fractions as 5.87 emu g^{-1} and 0.96 emu g^{-1}, respectively, while H_c value as 215.19 Oe. FE testing assured 68.42% of ferroelectric efficiency with $W_R = 3.43 \times 10^{-4}$ mJ cm^{-3} for $x = 0.06$ substitutional contents. ME coupling analysis verified MF behavior of tri-phase composites by linear trends. Looking ahead in the future, computational theoretical modelling and the computed parameters are paving a path for as-synthesized composites towards the fabrication of memory as well as modern energy storage devices.

Data availability

Data will be available on request.

Conflicts of interest

The authors declare that there are no financial or any other type of conflicts of interest to declare.

Acknowledgements

The authors would like to acknowledge the Researchers Supporting Project number (RSP2024R71), King Saud University, Riyadh, Saudi Arabia.

References

1 A. Ouertani, Z. Abdelkafi, H. Khemakhem and N. Randrianantoandro, *RSC Adv.*, 2024, **14**(20), 14080–14090.
2 S. Lan, C. Yu, F. Sun, Y. Chen, D. Chen, W. Mai and M. Zhu, *Nano Energy*, 2022, **93**, 106792.
3 M. M. Arman, *Appl. Phys. A-Matter*, 2023, **129**(6), 400.
4 N. A. Spaldin, *Philos. Trans. R. Soc., A*, 2020, **476**(2233), 20190542.
5 N. D'Souza, J. Atulasimha and S. Bandyopadhyay, *J. Phys. D: Appl. Phys.*, 2011, **44**(26), 265001.
6 D. Sando, A. Agbelele, C. Daumont, D. Rahmedov, W. Ren, I. C. Infante, S. Lisenkov, S. Prosandeev, S. Fusil, E. Jacquet, C. Carrétéro, S. Petit, M. Cazayous, J. Juraszek, J. M. Le Breton, L. Bellaiche, B. Dkhil, A. Barthélémy and M. Bibes, *Philos. Trans. R. Soc., A*, 2014, **372**(2009), 20120438.
7 I. Ragbaoui, S. Aydi, S. Chkoundali, M. Enneffati and A. Aydi, *RSC Adv.*, 2024, **14**(2), 1330–1340.
8 J. Wang, Z. Qing, X. Zhou, H. Zou, H. Li, A. Liu, S. Duan and Y. Li, *Ceram. Int.*, 2023, **49**(14), 23627–23633.
9 K. Yousefipour, R. Sarraf-Mamoory and S. Mollayousefi, *RSC Adv.*, 2022, **12**(43), 27868–27876.
10 S. B. Narang and K. Pubby, *J. Magn. Magn. Mater.*, 2021, **519**, 167163.
11 M. Khan, A. Mishra, J. Shukla, S. Bisen and P. Sharma, *AIP Conf. Proc.*, 2019, **2115**, 030107.
12 B. Dhanalakshmi, B. C. Sekhar, K. V. Vivekananda, B. S. Rao, B. P. Rao and P. S. Rao, *Appl. Phys. A-Matter*, 2020, **126**, 1–9.
13 M. Umair, A. Quader, M. Imran, M. A. Yaqub, S. M. Ramay and S. Atiq, *Ceram. Int.*, 2022, **48**(10), 14473–14480.
14 U. Ali, M. A. Khan, M. Mehak, M. T. Ansar, S. M. Ramay, E. A. Alghamdi, M. Shahabuddin and S. Atiq, *J. Alloys Compd.*, 2024, **970**, 172536.
15 P. Augustine, Y. Narayana and N. Kalarikkal, *Mater. Today: Proc.*, 2020, **25**, 208–212.

16 S. Moharana, T. Yadav, P. A. Alvi, A. Pathak and R. N. Mahaling, *J. Mater. Sci.: Mater. Electron.*, 2021, **32**, 6038–6046.
17 M. Mehak, M. A. Khan, U. Ali, A. Quader, M. Saleem, G. M. Mustafa, A. S. Haidyrah and S. Atiq, *Ceram. Int.*, 2021, **47**(15), 21688–21697.
18 K. Sreekanth, B. Dhanalakshmi and D. Madhavaprasad, *J. Indian Chem. Soc.*, 2022, **99**(7), 100565.
19 M. A. Khan, K. Shahbaz, G. M. Mustafa, S. M. Ramay, S. Naseem and S. Atiq, *J. Alloys Compd.*, 2023, **947**, 169571.
20 N. Patel, A. L. Srivastav, A. Patel, A. Singh, S. K. Singh, V. K. Chaudhary, P. K. Singh and B. Bhunia, *Environ. Sci. Pollut. Res.*, 2022, **29**(46), 69137–69152.
21 P. Piza-Ruiz, D. Avila-Ramos, A. Saenz-Trevizo, O. Solís-Canto, P. Amézaga-Madrid and M. Miki-Yoshida, *Ceram. Int.*, 2021, **47**, 18969–18976.
22 X. Hu and T. Suzuki, *Materials*, 2023, **16**(20), 6713.
23 E. Paradisi, M. Lassinantti Gualtieri, P. Veronesi, V. Dami, G. Lorenzi, A. Cioni, G. Baldi and C. Leonelli, *ACS Appl. Nano Mater.*, 2023, **6**(7), 5448–5459.
24 A. K. Bhakta, Y. Snoussi, M. E. Garah, S. Ammar and M. M. Chehimi, *C*, 2022, **8**(3), 46.
25 F. Deeba, A. K. Gupta, V. Kulshrestha, M. Bafna and A. Jain, *J. Mater. Sci.: Mater. Electron.*, 2022, **33**(30), 23703–23713.
26 F. Afzal, M. T. Ansar, A. S. Haidyrah, M. A. Khan, G. M. Mustsfa, M. Saleem and S. Atiq, *J. Alloys Compd.*, 2021, **888**, 161516.
27 B. D. Cullity, *Elements of X-ray Diffraction*, Addison-Wesley Publishing, 1956.
28 C. F. Holder and R. E. Schaak, *ACS Nano*, 2019, **13**(7), 7359–7365.
29 S. Nasiri, M. Rabiei, A. Palevicius, G. Janusas, A. Vilkauskas, V. Nutalapati and A. Monshi, *NanoTrends*, 2023, **3**, 100015.
30 H. Ayub, L. A. Khan, E. McCarthy, I. U. Ahad, K. Fleischer and D. Brabazon, *Metals*, 2022, **19**, 208–219.
31 R. K. Rajaboina, U. K. Khanapuram, V. Vivekananthan, G. Khandelwal, S. Potu, A. Babu, N. Madathil, M. Velpula and P. Kodali, *Small*, 2023, 2306209.
32 S. Kavitha and M. Kurian, *J. Alloys Compd.*, 2019, **799**, 147–159.
33 M. M. Kumar, V. R. Palkar, K. Srinivas and S. V. Suryanarayana, *Appl. Phys. Lett.*, 2000, **76**(19), 2764–2766.
34 U. Waqas, M. U. Salman, M. A. Khan, S. M. Ramay, F. Ahmad, S. Riaz and S. Atiq, *J. Mater. Sci. Technol.*, 2024, **29**, 2971–2979.
35 M. Luqman, R. Shazaib, A. Raza, M. A. Khan, M. A. Shar, S. M. Ramay, S. Riaz and S. Atiq, *J. Magn. Magn. Mater.*, 2023, **587**, 171361.